PAPER

Check for updates

AI based image analysis of red blood cells in oscillating microchannels†

Andreas Link, [ID] Irene Luna Pardo, [ID] Bernd Porr [ID] and Thomas Franke [ID] *

The flow dynamics of red blood cells *in vivo* in blood capillaries and *in vitro* in microfluidic channels is complex. Cells can obtain different shapes such as discoid, parachute, slipper-like shapes and various intermediate states depending on flow conditions and their viscoelastic properties. We use artificial intelligence based analysis of red blood cells (RBCs) in an oscillating microchannel to distinguish healthy red blood cells from red blood cells treated with formaldehyde to chemically modify their viscoelastic behavior. We used TensorFlow to train and validate a deep learning model and achieved a testing accuracy of over 97%. This method is a first step to a non-invasive, label-free characterization of diseased red blood cells and will be useful for diagnostic purposes in haematology labs. This method provides quantitative data on the number of affected cells based on single cell classification.

Introduction

Blood tests still play a major role in diagnostics since samples are easy to obtain and are routinely used for analysis in clinical and general practice settings.[1] Red blood cells (erythrocytes) form by far the major component of whole blood (about 50%) and have been used as biological indicators for several diseases such as sickle cell anaemia, spherocytosis, beta-thalassemia, malaria,[2,3] hypercholesterolemia[4,5] and many others. In many of these diseases the shape of the erythrocyte is altered, so simple optical microscopical examination and cell counting allows quantitative analysis in stasis *e.g.*, in a blood smear. The adopted shape depends on mechanical properties of the cell and the external strain. In hydrodynamic flow, there have been various shapes reported *in vivo* as well as *in vitro*. For healthy cells these encompass discocytes, parachutes and slipper-like shapes and echinocytes, spherocytes, *etc.* for diseased cells. However, not all cells of a sample are in the same shape condition, due to variances in mechanical properties within the cell population. Even within one blood sample there exists a variance of mechanical properties of the erythrocyte since for example cells alter their properties and size during their ~120 days lifetime of circulation in the organism.[6] Red blood cells (RBCs) in microflow conditions have been analysed both in experiments[7] and theory.[8] Most of the studies are in capillary flow, yet some research was done on more complex geometries to reveal the shape relaxation dynamics.[9,10]

Based on viscoelastic models the experimentally observed cells could be reproduced and variation of mechanical parameters (viscoelastic moduli) were determined has also demonstrated that transitions in between these cell shapes can occur. However, in experimental settings it is still challenging to distinguish between populations of red blood cells from different samples, such as diseased cells and healthy cells.

In AI based red blood cell classification most of the prior work[11-13] distinguished between populations of cells with the associated problems mentioned above and in addition poses technical problems when employing segmentation techniques to isolate individual blood cells which are error prone and computationally intensive. Because there is a strong interest in the viscoelastic properties of the red blood cells often only their shape has been analysed but not the healthiness of the cells.[14,15] The use of a channel to probe the mechanical properties of the red blood cells in conjunction with AI to detect a disease has, to our knowledge, only attempted once.[16]

Here, we demonstrate an AI based image analysis using TensorFlow that can decide between native, untreated red blood cells and red blood cells with chemically altered mechanical properties to mimic disease.[17-24] Unlike the other studies mentioned before, we do not analyse the contour or shape of the cell to model the cell mechanics but train a TensorFlow implemented AI model with a large number of images from native and treated cells. The model is trained for 10 epochs and achieves a high training and validation accuracy already after ~5 epochs, making is very efficient. Experimentally, we use a microchannel with oscillating width to transiently deform cells to capture both, the elastic, and the viscous properties. Our device presents a method that can distinguish a population of cells which are not obvious by simple inspection by eye. It is ready to be used for disease diagnosis and analysis of the severity of a disease by providing quantitative

Division of Biomedical Engineering, School of Engineering, University of Glasgow, Oakfield Avenue, G12 8LT Glasgow, UK. E-mail: Thomas.franke@glasgow.ac.uk

results on the frequency of affected cells and enables an end-to-end classification of red blood cells without understanding the biomechanical differences between the classified cells in detail.

Results

Microfluidic procedures/setup

We probe red blood cells in flow with periodically oscillating flow velocities in a zigzag-shaped microchannel. The channels are fabricated using standard soft-lithography and mounted on an inverted fluorescence microscope. Videos of cells flowing through the channel are recorded with a high-speed camera (Photron, UX50). Red blood cell samples are prepared from whole blood by centrifugation and incubation steps with chemicals for modification of their mechanical properties (see material and methods section). We use a diluted red blood cell suspension in PBS buffer with a haematocrit (Ht) of Ht = 0.5% and inject it into the inlet of the microfluidics device using a pressure driven system, controlling the pressure drop between inlet and outlet. Cells then enter a zigzag-shaped region that is in the field of view of a 60× objective as shown in Fig. 1. To avoid large sections of videos without cells and to reduce memory consumption at the low chosen, we trigger the recording of videos by a hardware trigger. Therefore, we use a laser to excite (488 nm) a fluorescent marker in the red blood cell and detect the emitted (525 nm) fluorescence signal with a photomultiplier tube (PMT). In this way we record cell sequences of 60 and 40 frames per cell. We record 248 sequences and then transfer the batch of data from the fast camera RAM to the computer hard drive for post-processing.

Video processing

Three batches of 248 sequences each were recorded for healthy cells which results in a total of 744 video sequences of native red blood cells (the first two sequences where removed). Two batches of 248 sequences each were recorded for chemically modified cells which resulted in a total of 496 video sequences. Fig. 2 shows how the training data has been extracted from the raw video sequences. Fig. 2A shows a snapshot of one clip where the cells are flowing from the left to the right. Here, the cell has already progressed to the 2nd narrow section of the channel. Since we are interested how the zigzag-channel impacts on the
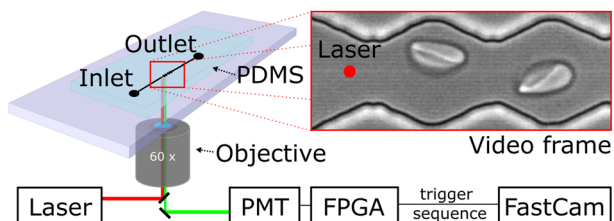

Fig. 1 Schematic of the microfluidic setup mounted on an inverted fluorescence microscope: RBCs entering the device and flow into the region of oscillating width and adopt their shape. Videos are taken with a fast camera and recording is triggered by cell passing a photoelectric barrier and rapid analysis in a photomultiplier tube.
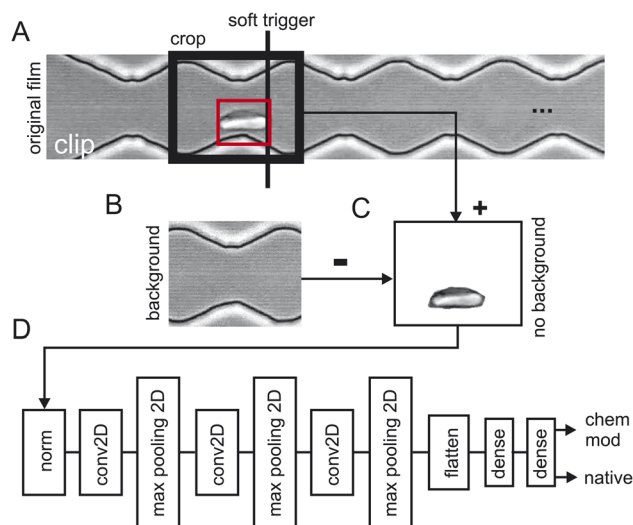

Fig. 2 2 Data processing pipeline. (A) Single frame from a video clip with a red blood cell in the red boundary box touches the "soft trigger" (black line) which then leads to the extraction of the image in the area "crop" (black box). (B) Background of the cropped area from (A) by taking a video frame from the video clip without a red blood cell. (C) Background subtraction of (B) subtracted from (C) and taken the absolute value. (D) TensorFlow layers: "norm": RGB value normalisation to 0.01, "conv2D": standard 2D convolutional layer, "max pooling": standard 2D max pooling, "dense": standard dense layer. The final layer has two outputs: one for the detection probability of a native red blood cell and one for the chemically modified one.

cell's behaviour and shape, we have defined a "soft trigger" where a snapshot for training is used. One can think of the soft trigger as a finishing line in a race.

As an example, we have shown one soft trigger when the cell in the red square has just arrived at a narrow section and has touched the soft trigger. A 2nd soft trigger has also been established (not shown) when the cell has arrived at a wide section and thus, we have two soft triggers: one for taking a snapshot in the narrow section and one for the section. Once the cell has been detected a snapshot is taken of the size of the crop window indicated with "crop" in Fig. 2A. As a next step the background was obtained (Fig. 2B) and subtracted (Fig. 2C) to prevent TensorFlow from learning features of the background instead of that of the red blood cells. Since the cell flows through the image from left to right, we can take the background for the left half from the final frames of a clip and the background from the right half from the first frames of the clip. Splicing these two halves together gives the background which can then be used in Fig. 2C to obtain a background-free cell image.

Data analysis and decision making with TensorFlow

The video processing pipeline described above uses three batches of 248 images (one image per sequence) of native red blood cells and two batches of 248 images of chemically modified red blood cells for training. For training the model every image is labelled of either being healthy or diseased. This results in 5x248 images/label-pairs. These pairs are then

shuffled randomly for training and then fed into TensorFlow (Fig. 2D). This is a standard network topology as suggested by TensorFlow/Keras to do image classification. The network has two outputs, one gives the probability of being a native cell and one the probability of being a chemically modified one. Training was performed with 10 epochs and the test accuracy evaluated with two separate batches of clips not being part of the training: 492 images of healthy red blood cells and 111 images of diseased cells. These two subpopulations where then sent into TensorFlow for training (80%) and validation (20%) which is described next.

Comparison of frame location in the microfluidic channel

To investigate the impact of the position of the cell in the microchannel we created two datasets of red blood cell images and fed them into TensorFlow – one with the red blood cells detected in the widening section of the microchannel and another one with the red blood cells in the narrow section as shown in Fig. 3. The goal of training is to have for a two-output classifier one output close to one and its other output close to zero so that either the "native" output becomes one or the "chemically modified"

becomes one but never both. TensorFlow training and validation on the dataset containing images from the narrow part of the channel is shown in Fig. 3A: on the left the training and validation accuracy is shown and on the right the training and validation loss is shown. Both training and validation accuracy reach 99% after 5 epochs and stabilise there. The same applies for the training and validation loss which reach their minimum after 5 epochs. Training using images from the wide section (Fig. 3B) of the microchannel result is remarkably similar behaviour: both the training accuracy and the validation accuracy converge to over 99% after 5 epochs. Also, the training loss and validation loss reach their minima in a similar way as the training in the narrow section.

After training the TensorFlow model was presented with test data which the network has not yet seen: 492 clips of native red blood cells and 111 clips of chemically modified cells. The testing accuracy at the narrow section was 98% and for the wide one 97%. Fig. 3C/D show the testing results for the dataset generated at the narrow section of the channel and Fig. 3E/F at the wide section of the channel. Every row shows three examples of red blood cells and their detection probability against the ground truth: true native or true chemically modified. Remember that training forces the network to clearly output a one for its detection category. For example, in Fig. 3C the ground truth is "native" and the network outputs a one for native, indicated as "N" under the green bar. Then in Fig. 3D the cells were chemically modified, and the network classified them all with very high confidence as chemically modified ("C"). Fig. 3E/F now shows the same as above but for the wide section of the channel. Again, true native ones are detected as native without any doubt and reflects the 97% of the testing accuracy. The truly chemically modified ones were also detected with ease. Having just two categories being native or chemically modified allows a simple comparison which is robust with one category being almost zero and the other almost one.

Material and methods

Microfluidic device preparation

Microfluidic channels are fabricated using soft lithography.[25,26] Briefly, the channel structure is designed in CAD program and transferred to a chromium mask (ML&C GmbH). The zigzag-shaped channel has a periodicity of 20 μm, and an amplitude of 20 μm. The narrow part of the channel is 10 μm and the wide part is 20 μm in width (for details see sketch in the ESI†). To structure of the mask is transferred to a silicon wafer coated with 10 μm SU8-3010 photoresist that defines the height of the channel (Microchem, SU8 3000 series) using a mask aligner (MA6, Süss MicroTec). After developing with (Microposit™EC Solvent, Shipley), the structured SU8 acts as a template to fabricate PDMS moulds (PDMS, Sylgard™ 184 Silicone Elastomer Kit). The fluid PDMS is poured onto the template and cured for 4 h in an oven at 75 °C. The ratio of elastomer base to curing agent is 10 : 1.

We punch holed into the cured PDMS mould to connect inlet and outlet to the tubing. The PDMS is covalently bonded onto a microscope slide using oxygen plasma.
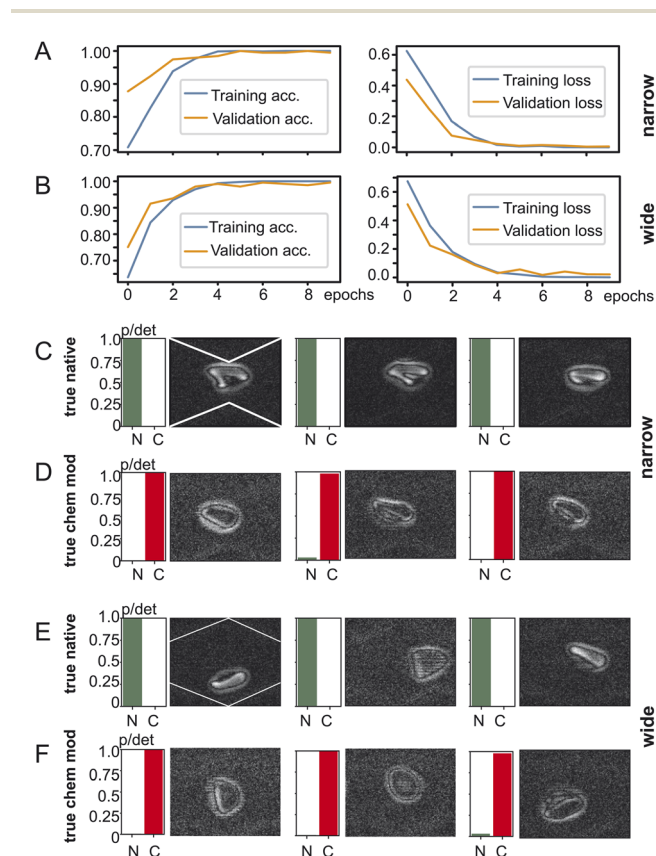

Fig. 3 TensorFlow training behaviour and results. (A) Training and validation loss for the narrow part of the microchannel and for the wide part (B) of the microchannel. Classification results for the narrow section of the microchannel for (C) native red blood cells and (D) chemically modified red blood cells. Classification results for the wide section of the microchannel for (E) native red blood cells and (F) chemically modified red blood cells. "N": native, "C": chemically modified, "p/det": detection probability.

RBC preparation

Whole blood was obtained from healthy donors (Research Donors, Cambridge Bioscience) and washed three times in a phosphate-buffered saline solution (PBS 1×, pH 7.4, 307 mOsm L^{-1}, Gibco Life Technologies). After each washing step, the sample was centrifuged for 5 minutes at 2500 rpm (mini spin plus centrifuge, Eppendorf), and the white buffy coat and supernatant were removed.

For the native red blood cell sample, we used 10 μL of concentrated RBC pellet from the bottom of the reaction tube and incubated in 0.5 mL green-fluorescent calcein-AM solution (5 μM, Invitrogen) for 30 minutes at 37 °C, followed by three washes with PBS.

For the chemically modified RBC experiments, we first incubate the red blood cells in formaldehyde solution before we stain the cells. Briefly, 10 μL of the pellet were incubated in 0.37% formaldehyde solution (Sigma-Aldrich) for 10 min at room temperature. The cell suspension was then washed three times before stained in calcein-AM as described above.

To avoid cell sedimentation during the experiment, the cells were suspended in a density-matched solution using a density gradient solution (OptiPrep Density Gradient Medium, Sigma Life Science). Optiprep is a sterile non-ionic solution of 60% (w/v) iodixanol in water. Additionally, bovine serum albumin (BSA, Ameresco) was used to prevent cell adhesion to each other and the microchannel walls. The stock density matched solution was prepared by mixing 945 μL of OptiPrep solution with 3035 μL of PBS and 40 mg BSA.

For the experiments 5 μL of the native or chemically modified cell suspension were mixed with 995 μL of the stock density matched solution and used as the stock solution with a haematocrit of 0.5%. The experiments were completed within a day of blood collection. The final density of this solution was ρ = 1.080 g mL^{-1} with an osmolarity of c_{osm} = 317 mOsm L^{-1}. The viscosity of this solution was determined after Ubbelohde to be η = 1.5 ± 0.1 mPa s.

The red blood cell suspension was pumped by a pressure driven flow using a pressure transducer (MarshBellofram, USA) and a pressure of p = 20 mbar at cell velocities in range from 1.3–8 mm s^{-1}. Due to the Poiseuille-like flow cells flowing close to the wall are slower than cells in the centre of the channel. The average velocity of the red blood cells measured is v_{RBC} =5.1 ± 2.0 mm s^{-1}. The flow velocity is not constant and does change along the channel because of the alternating width and across the channel due to the Poiseuille-profile. Similarly, the flow rate is variable. However, to estimate typical shear forces on the cell we estimate an effective shear rate from an average channel width of w_{av} = 15 μm and the average velocity to be $\dot{\gamma}_{eff}$ = $2v_{RBC}w_{av}$ = 680 s^{-1}. From the shear rate and the viscosity of the density matched solution η = 1.5 mPa s we estimate an effective shear stress to be τ_{eff} = $\eta \times \dot{\gamma}$ =1.0 Pa.

Python code

The red blood cells videos consist of multiple sequences conjugated after each other triggered by the fluorescence detector described in Fig. 1. The number of sequences in each video can vary in the number of frames and is specified in the code for the different videos used. We use two "finishing lines" at different positions in the oscillating channel where we wanted to capture images of cells at the wide and narrow sections. The finishing lines were different for wide and narrow section at each of the videos and it was inputted in the code specific for the different videos as before.

To detect the cells at these finishing lines, we used OpenCV background subtractor, a Gaussian Mixture-based background/foreground segmentation, with a history of 100 and varThreshold of 20. We exclusively applied this only to the specific detection area which was determined by the finishing line parameter we had specified. The detection area was defined by a y range of (10 110) and an x range from the finishing line to the finishing line plus 250. Then, we used OpenCV function "findcontours" to create contours around the moving cells in that detection area. We defined an area threshold of 20 px^2 enclosed by these contours to identify a cell. If a cell passes the detection area and is above the set threshold the frame number is recorded and an image of the cell is extracted. In this way the function "findcontours" is only used to determine the soft-trigger as shown in Fig. 2 and no information on the contour is used in the AI categorization model.

The resulting images were cropped to a size of 120 × 150 pixels, with a cropping range of 0 to 120 for height and from the finishing line minus 80 to the finishing line plus 70 for the width. Therefore, images were of a shape of (120,150,3).

For our neural network, we used Keras sequential model with 10 layers. The first layer is used to rescale and normalize the input data. In the second layer a 2D convolution layer is used with 16 filters to detect different features in the input image. The next layer, the Maxpooling2D layer, reduces the spatial dimensions of the data, controlling overfitting and reduces the computational load. In the fourth layer another 2D convolutional layer is used but with more filters as before, with 64 as the number of output filters. Then another Maxpooling2D layer to reduce the dimensions of the data is used. To prepare the data for the upcoming dense layers the multidimensional output from the previous layers is flattened into a one-dimensional vector. For the two dense layers we used first 128 units per neuron to learn the complex relationship between the flattened features followed by the last layer, another dense layer with two units representing the output classes: "native" and "chemically modified". To extract all pixel information from the images we used in the 2D convolutional layers a stride parameter of (1,1) and a kernel size of (3,3). Finally for the training, we passed through the entire training dataset ten times (10 epochs) in batch sizes of 32 samples where after each batch the gradients were updated. A schematic representation of the network is shown in Fig. 2D.

Discussion

In this study we have used periodically oscillating zigzag-shaped microchannels to probe RBCs. Compared to many other studies the spatially alternate design enables the interrogation of viscous cell properties. In contrast, RBCs in cylindrical capillary

flow adopt a constant shape and neither dynamic, viscous properties of the RBC cell membrane nor the cytosol enter because the cell moves as a fixed object in flow. Here, we probed cells at two separate locations in microflow, at the widening and the constriction. In between these extrema, the RBCs adopt an intermediate shape. The transition between these shapes in the wide and narrow section is controlled by the relaxation time of the RBC as given by the ratio of viscous to elastic parameters. Here, we tested native and chemically modified RBCs using formalin at 0.3% volume ratio (formaldehyde in water solution). Formalin is a fixation agent and non-specifically cross-links proteins in the RBC thereby modifying the viscoelastic, mechanical properties of the cell. Similar to glutaraldehyde (GA), the aldehyde group binds and can interlink amino acids of proteins and thereby mechanically stabilize the RBC membrane. In GA mediated mechanical modification, the GA can exist as a monomeric or polymeric form, both of which bind to amino acids. Therefore, GA can link proteins over a variable distance depending on the length of the polymer. Even though formalin can also form formaldehyde polymers, the mechanically reactive form with an aldehyde group is the monomer, *i.e.* methylene hydrate. Only as monomer it can bind to proteins to form a methylene cross-link. Therefore, the potential for cross-linking with GA is much larger, firstly because of its two aldehyde binding sites and secondly due to the variable lengths.[23] Hence, the effect of formalin is milder and slower than the one of GA, facilitating chemical control of mechanical RBC properties. However, due to the small size formalin has been reported to have a much higher permeation rate compared to GA.[27] It can potentially enter the RBC and link proteins in the cytosol, such as hemoglobin.[27]

In AFM studies an increase in elastic modulus depending on GA concentration has been reported as well as a reduction in deformability (elongation index).[23] AFM measurements using formalin at a concentration of 5% have revealed a 10-fold increase in Young modulus as compared to untreated cells.[28] The difference in stiffness leads to less deformation and a lower elongation index as obtained from a shape analysis.[29]

Stiffening of RBC membrane has also been achieved by incubation in diamide.[24,30,31] However, diamide has been reported to only rigidify the membrane stiffness and fluidity. It provides disulphide bridges between specific thiol-group containing amino-acids (cystine, methionine) and has a minor effect on the cytosol. Its effect has been studied in microflow analysing the shape changes by using the cell width to length ratio.[32]

In our experiments, the changes in viscoelastic properties due to chemical treatment with formalin 0.3% are expected to affect the morphology of the RBC in flow. However, we could not detect any apparent shape changes in our micrographs by eye or simple analysis such as analysing the deformation index or projected area.

Instead of analysing the RBC shape and contour as we have done in previous studies,[33,34] here we have taken an AI based approach.[35]

A few other authors have used AI based analysis in microfluidics channels. Lamoureux *et al.*[36] used a microfluidic ratchet channel to sort highly deformable RBCs and trained the machine learning on the isolated cells. Darrin *et al.*[44] have used millimetre sized channels and observed red blood cells near the wall at shear rates of 10 s^{-1} to study the motion from tumbling to tank treading. The channel size used by Recktenwald *et al.*[37] and Kihm[14] *et al.* have similar dimensions as our geometry and both are operating in the same velocity range of up to 10 mm s^{-1}. However, they use a straight channel and different flow rates to investigate the shape transition of individual red blood cells and therefore their device is mainly sensitive to elastic parameters.

Alkrimi *et al.*[15] have classified RBCs using machine learning principal component analysis to reduce the correlation of features. Yet, the morphological analysis was done on a blood smear and not involving microfluidic channels.

Using a TensorFlow based machine learning we categorize native and chemically treated cells with high precision and with less training data required because we use a pretrained model.

This goes beyond current literature that probe red blood cells in simple capillary flow.[16]

We examined how the position of cells within an oscillating microchannel affects the outcome of the categorization. Two sets of red blood cell images were used, one in the channel's wider section and the other in the narrower section. Using TensorFlow, an image classifier with two outputs was trained and its objective was to generate one output close to one while maintaining the other output close to zero, thus, effectively distinguishing between "native" and "chemically modified" cells. The training accuracy for images of both section in the microchannel exceeded 99% after only five epochs, demonstrating the fast and efficient training convergence of the model. Similarly, the validation accuracy converges rapidly as shown in Fig. 3A and B. As a second indicator we used the training and validation loss, a parameter that quantifies how bad the prediction of the model is (penalty for poor prediction). Both indicators rapidly converge to small value indicating a very good prediction of the model. In both, the narrow and wide part of the channel, the validation and training accuracies and loss are monotonous increasing and decreasing, respectively and the fluctuation of their values with epochs is small. The value of all indicators plateau within about 5 epochs, again showing a very efficient categorization.

The trained model was then tested with previously unseen data of native and chemically modified cells and yielded a 98% accuracy rate for the narrow section and 97% for the wide section. Apparently, the binary categorization of cells does only weakly depend on the position of the cell and suggests that the selection of the position is not critical to the prediction of the image-based AI model.

Central to red blood cell diagnostics is the analysis of their deformability and, thus, their ability to form different shapes.[16,36] For example, Kihm *et al.* divided the cells in two groups called "Slippers" and "Croissants",[14] implemented a CNN (Convolutional Neural Network) to train 4000 images and classify the RBCs uniquely based on their shape characteristics. Considering the increasing demand for advancements and the potential for significant impact and popularity in this field,

Recktenwald *et al.*[37] and its follow-up study[38] adopted the approach, proposed by Kihm *et al.* and Alkrimi *et al.*,[14,15] to benchmark different AI techniques classifying RBCs and similarly to Kihm *et al.*,[14] the classification was based fully on morphology. Lee *et al.*[39] uses not just shape but also texture features to classify normal and abnormal RBCs and similarly to Das *et al.*,[12] they classify cells in more than two categories. However, overall, these studies employ an intermediate step by first or exclusively focussing on morphology and then feeding the pre-processed data into the final classifier for diagnosis. However, this assumes that one knows which deformation, shape or texture relates to a diseased cell and which one to a healthy one. In contrast, we do pixel-to-disease-classification (*i.e.*, end to end) where the deep net learns the distinguishing features by itself without 1st hand-crafting features and only then feeding them into a classifier.

Often raw microscopic images taken contain a large amount of red blood cells which requires a segmentation process to extract individual images.[16,39] Due to the segmentation processes and individual image extraction, the quality of the image is often seen reduced and as a consequence degrades the classification accuracy. Other approaches to work with images of many red blood cells are the Circular Hough transform[40] or region-based segmentation (ORBS).[13] Das *et al.*[12] also studies segmentation of RBCs in image classification and similarly to the other studies[40] and the study of Shemona *et al.*,[13] the images analysed also contain many RBCs. In contrast to these studies our work directly captures single red blood cells passing through the microchannel and is not affected by image degradation, low resolution after cropping or wrong segmentation.

AI can be used to classify RBCs into more than two categories,[12,39] for example Malaria, Thalassaemia, other abnormal and normal.[11] In our study we have used two categories as a proof of concept but the TensorFlow classifier can take any number of classes where the only limit is the available computing power and GPU memory. Future work will use more than two categories.

Confounding factors are a significant challenge in any AI based learning algorithm which is at risk of learning just trivial and superficial features from the training data. For instance, Zech *et al.* explains that CNNs may not effectively identify disease-specific finings but rather exploit confounding information.[41] This crucial issue is only addressed by Rizzuto *et al.* which tries to eliminate any confounding structures cropping the video to extract only a limited area of interest.[16] No study has explored the effect of confounding factors such as focal plane on image classification of RBCs. In this study we discovered that AI would use the focal plane to distinguish between native and chemically modified RBCs when using one focal plane for the native ones and one for the diseased ones. To overcome this problem, we mixed images captured at different focal planes and, in addition, removed the background from the images.

Conclusion

We have demonstrated an end-to-end classification of two populations of red blood cells with an open-source AI image analyser based on TensorFlow. Cells of both populations flow through a microchannel and images are taken at specific locations in the channel. The model very effectively classifies the cell into native and chemically modified and reaches a high level of accuracy already after 5 epochs. The fully trained model was tested with an unknow sample, and the testing accuracy was 98% and 97% in the narrow and wide section of the channel, respectively. The high level of accuracy and the quickly converting low level of testing and validation loss justifies our approach. In the future we aim to extend the analysis to other blood samples from patients for disease diagnostics and combine the analysis with droplet based microfluidics and red blood cell encapsulation[42] as well as acoustic approaches for viscoelastic cell classification.[43]

Conflicts of interest

There are no conflicts to declare.

Acknowledgements

References

1 M. Gary, G. Knight and A. D. Blann, *Haematology*, Oxford University Press, Oxford, 3rd edn, 2021.

2 T. M. Geislinger, S. Chan, K. Moll, A. Wixforth, M. Wahlgren and T. Franke, *Malar. J.*, 2014, **13**, 375.

3 H. A. Cranston, C. W. Boylan, G. L. Carroll, S. P. Sutera, J. R. Williamson, I. Y. Gluzman and D. J. Krogstad, *Science*, 1984, **223**, 400–403.

4 M. Kohno, K. Murakawa, K. Yasunari, K. Yokokawa, T. Horio, H. Kano, M. Minami and J. Yoshikawa, *Metabolism*, 1997, **46**, 287–291.

5 J. Radosinska and N. Vrbjar, *Physiol. Res.*, 2016, **65**, S43–S54.

6 M. J. Simmonds, H. J. Meiselman and O. K. Baskurt, *J. Geriatr. Cardiol.*, 2013, **10**, 291–301.

7 G. Tomaiuolo, M. Simeone, V. Martinelli, B. Rotoli and S. Guido, *Soft Matter*, 2009, **5**, 3736–3740.

8 H. Noguchi and G. Gompper, *Proc. Natl. Acad. Sci. U. S. A.*, 2005, **102**, 14159–14164.

9 S. Braunmüller, L. Schmid and T. Franke, *J. Phys.: Condens.Matter*, 2011, **23**, 184116.

10 S. Braunmüller, L. Schmid, E. Sackmann and T. Franke, *Soft Matter*, 2012, **8**, 11240–11248.

11 Y. Hirimutugoda and G. Wijayarathna, *Sri Lanka J. Biomed. Inform.*, 2010, **1**, 35.

12 D. K. Das, C. Chakraborty, B. Mitra, A. K. Maiti and A. K. Ray, *J. Microsc.*, 2013, **249**, 136–149.

13 J. S. Shemona and A. K. Chellappan, *IET Image Process.*, 2020, **14**, 1726–1732.

14 A. Kihm, L. Kaestner, C. Wagner and S. Quint, *PLoS Comput. Biol.*, 2018, **14**, e1006278.

15 J. A. Alkrimi, S. A. Tome and L. E. George, *Eur. J. Sci. Res.*, 2019, **4**, 17–22.

16 V. Rizzuto, A. Mencattini, B. Álvarez-González, D. Di Giuseppe, E. Martinelli, D. Beneitez-Pastor, M. del M. Mañú-Pereira, M. J. Lopez-Martinez and J. Samitier, *Sci. Rep.*, 2021, **11**, 13553.

17 J. Dupire, M. Socol and A. Viallat, *Proc. Natl. Acad. Sci. U. S. A.*, 2012, **109**, 20808–20813.

18 G. Tomaiuolo, L. Lanotte, R. D'Apolito, A. Cassinese and S. Guido, *Med. Eng. Phys.*, 2016, **38**, 11–16.

19 G. Tomaiuolo, *Biomicrofluidics*, 2014, **8**(5), 051501.

20 G. Tomaiuolo and S. Guido, *Microvasc. Res.*, 2011, **82**, 35–41.

21 L. Boas, V. Faustino, R. Lima, J. Miranda, G. Minas, C. Fernandes and S. Catarino, *Micromachines*, 2018, **9**, 384.

22 G. Tomaiuolo, M. Simeone, V. Martinelli, B. Rotoli and S. Guido, *Soft Matter*, 2009, **5**, 3736.

23 A. Abay, G. Simionato, R. Chachanidze, A. Bogdanova, L. Hertz, P. Bianchi, E. van den Akker, M. von Lindern, M. Leonetti, G. Minetti, C. Wagner and L. Kaestner, *Front. Physiol.*, 2019, **10**, DOI: 10.3389/fphys.2019.00514.

24 A. M. Forsyth, J. Wan, W. D. Ristenpart and H. A. Stone, *Microvasc. Res.*, 2010, **80**, 37–43.

25 Y. Xia and G. M. Whitesides, *Annu. Rev. Mater. Sci.*, 1998, **28**, 153–184.

26 D. Qin, Y. Xia and G. M. Whitesides, *Nat. Protoc.*, 2010, **5**, 491–502.

27 J. A. Kiernan, *Microsc. Today*, 2000, **8**, 8–13.

28 T. G. Kuznetsova, M. N. Starodubtseva, N. I. Yegorenkov, S. A. Chizhik and R. I. Zhdanov, *Micron*, 2007, **38**, 824–833.

29 T. Go, H. Byeon and S. J. Lee, *Sci. Rep.*, 2017, **7**, 41162.

30 N. Mohandas, M. R. Clark, M. S. Jacobs and S. B. Shohet, *J. Clin. Invest.*, 1980, **66**, 563–573.

31 I. Safeukui, P. A. Buffet, G. Deplaine, S. Perrot, V. Brousse, A. Sauvanet, B. Aussilhou, S. Dokmak, A. Couvelard, D. Cazals-Hatem, O. Mercereau-Puijalon, G. Milon, P. H. David and N. Mohandas, *Blood Adv.*, 2018, **2**, 2581–2587.

32 M. Faivre, C. Renoux, A. Bessaa, L. Da Costa, P. Joly, A. Gauthier and P. Connes, *Front. Physiol.*, 2020, **11**, 1–10.

33 H. Noguchi, G. Gompper, L. Schmid, A. Wixforth and T. Franke, *EPL*, 2010, **89**, 28002.

34 S. Braunmüller, L. Schmid and T. Franke, *J. Phys.: Condens.Matter*, 2011, **23**, 184116.

35 J. Yim, R. Chopra, T. Spitz, J. Winkens, A. Obika, C. Kelly, H. Askham, M. Lukic, J. Huemer, K. Fasler, G. Moraes, C. Meyer, M. Wilson, J. Dixon, C. Hughes, G. Rees, P. T. Khaw, A. Karthikesalingam, D. King, D. Hassabis, M. Suleyman, T. Back, J. R. Ledsam, P. A. Keane and J. De Fauw, *Nat. Med.*, 2020, **26**, 892–899.

36 E. S. Lamoureux, E. Islamzada, M. V. J. Wiens, K. Matthews, S. P. Duffy and H. Ma, *Lab Chip*, 2022, **22**, 26–39.

37 S. M. Recktenwald, M. G. M. Lopes, S. Peter, S. Hof, G. Simionato, K. Peikert, A. Hermann, A. Danek, K. van Bentum, H. Eichler, C. Wagner, S. Quint and L. Kaestner, *Front. Physiol.*, 2022, **13**, DOI: 10.3389/fphys.2022.884690.

38 S. M. Recktenwald, G. Simionato, M. G. M. Lopes, F. Gamboni, M. Dzieciatkowska, P. Meybohm, K. Zacharowski, A. von Knethen, C. Wagner, L. Kaestner, A. D'Alessandro and S. Quint, *Elife*, 2022, **11**, e81316.

39 H. Lee and Y.-P. P. Chen, *Pattern Recognit. Lett.*, 2014, **49**, 155–161.

40 H. A. Elsalamony, *Micron*, 2016, **83**, 32–41.

41 J. R. Zech, M. A. Badgeley, M. Liu, A. B. Costa, J. J. Titano and E. K. Oermann, *PLoS Med.*, 2018, **15**, e1002683.

42 H. Lu, O. Caen, J. Vrignon, E. Zonta, Z. El Harrak, P. Nizard, J.-C. Baret and V. Taly, *Sci. Rep.*, 2017, **7**, 1366.

43 A. Link and T. Franke, *Lab Chip*, 2020, **20**, 1991–1998.

44 M. Darrin, *Sci. Rep.*, 2023, **13**, 745.